Journal of Materials Chemistry A

ROYAL SOCIETY OF CHEMISTRY

PAPER

View Article Online
View Journal | View Issue

Cite this: *J. Mater. Chem. A*, 2023, **11**, 14025

A MOF vertical array enables continuous ion transport pathways with high throughput†

Shuxian Wang,‡ Zhongliang Li,‡ Fangying Shen,‡ Zhiqin Ruan, Yutong Huang, Yang Liu, Yan Liu, Luyi Chen,* Ya-Qian Lan* and Qifeng Zheng *

Received 22nd March 2023
Accepted 25th May 2023

DOI: 10.1039/d3ta01715j

rsc.li/materials-a

Metal–organic frameworks (MOFs) have attracted a great deal of attention as ion conductive materials to design high-performance composite solid electrolytes (CSEs). However, the sluggish Li^+ transport arising from the physical contact among MOF particles with numerous interfaces results in insufficient ionic conductivity and inhomogeneous Li deposition. Herein, a MOF array-based CSE is rationally proposed by embedding a MOF vertical array with bilayer polymer electrolytes. The MOF vertical array offers not only continuous ion transport pathways with high throughput and the shortest transport distance, but also open metal sites to anchor the anions and homogenize the Li^+ flux. Moreover, the bilayer polymer structure enhances the interfacial compatibility with the Li-metal anode and high-voltage cathode simultaneously. Consequently, the resulting MOF array CSE enables the stable cycling of a Li||Li symmetric cell for over 800 h and high-voltage Li||NCM cell at room temperature. Therefore, this work opens up a new frontier in engineering CSEs with MOF vertical arrays towards high-performance solid-state lithium batteries at room temperature.

1. Introduction

Lithium metal has been considered as the most promising anode for next-generation high-energy rechargeable lithium batteries due to its high theoretical specific capacity (3860 mA h g^{-1}) and lowest electrochemical potential (−3.04 V *vs.* standard hydrogen electrode).[1–4] However, the conventional liquid organic electrolyte can spontaneously react with the lithium metal anode,[5,6] resulting in low coulombic efficiency (CE), high interfacial resistance, uneven Li^+ deposition, and uncontrollable growth of lithium dendrites, which can further cause short-circuits with serious safety issues.[7,8] As a result, solid-state electrolytes (SSEs) have been gradually developed to address the aforementioned issues, owing to their desirable characteristics of being nonflammable and able to prevent the growth of lithium dendrites, as well as possessing a wide electrochemical voltage window.[9]

To date, various types of SSEs have been investigated, which can be classified into the following three categories, including inorganic solid electrolytes (ISEs), solid polymer electrolytes (SPEs), and composite solid electrolytes (CSEs).[10–14] ISEs, such as oxides (*e.g.*, $Li_7La_3Zr_2O_{12}$, LLZO)[15] and sulfides (*e.g.*, $Li_{10}GeP_2S_{12}$, LGPS[16]), possess the merits of high ionic conductivity at room temperature, good thermal stability and high Li^+ transference number,[17,18] while their brittle nature leads to poor interfacial contact and poor processability.[19] Meanwhile, SPEs composed of polymeric matrixes (*e.g.*, poly(vinylidene fluoride) (PVDF) or poly(ethylene oxide) (PEO)) with lithium salts have been widely studied because of their high flexibility, excellent interfacial stability, and versatile processibility. However, SPEs suffer from poor mechanical strength and low ionic conductivity at room temperature, which hinders their practical applications.[20–22] Consequently, there is growing interest in incorporating inorganic ionic conductors into polymeric

School of Chemistry, South China Normal University, 55 West Zhongsan Rd., Guangzhou 510006, Guangdong, China. E-mail: chenluyi@m.scnu.edu.cn; yqlan@m.scnu.edu.cn; qifeng.zheng@m.scnu.edu.cn

† Electronic supplementary information (ESI) available. See DOI: https://doi.org/10.1039/d3ta01715j

‡ S. Wang, Z. Li, and F. Shen contributed equally to this work.

Dr Qifeng Zheng is a Professor of Chemistry at South China Normal University. He received his BS degree in Chemistry from Xiamen University in 2012, and PhD degree in Materials Science from the University of Wisconsin–Madison in 2017. From 2018 to 2019, he served successively as a Project Researcher and JSPS Fellow in the Department of Chemical Engineering at The University of Tokyo. His research mainly focuses on developing high-performance electrolytes for rechargeable batteries with high energy density and high safety.

matrixes to produce CSEs, with the aim of combining the merits of ISEs and SPEs while overcoming their disadvantages.[23–25]

Recently, metal–organic frameworks (MOFs) have been used as a novel ionic conductor and have shown great potential as fillers to manipulate ion transport in CSEs.[26–28] Firstly, the high surface area of MOFs could improve interfacial contact with electrodes and electrolytes, endowing CSEs with low resistance. Secondly, the custom-made pores and the open metal sites (OMSs) from the functional framework of MOFs could capture the anions of lithium salts through the sieving effect and Lewis acid–base interaction, resulting in rapid Li^+ transport and a high Li^+ transference number. Thirdly, the periodically ordered channels from MOFs could be helpful to achieve a homogeneous Li^+ flux and further regulate the homogeneous deposition of Li.

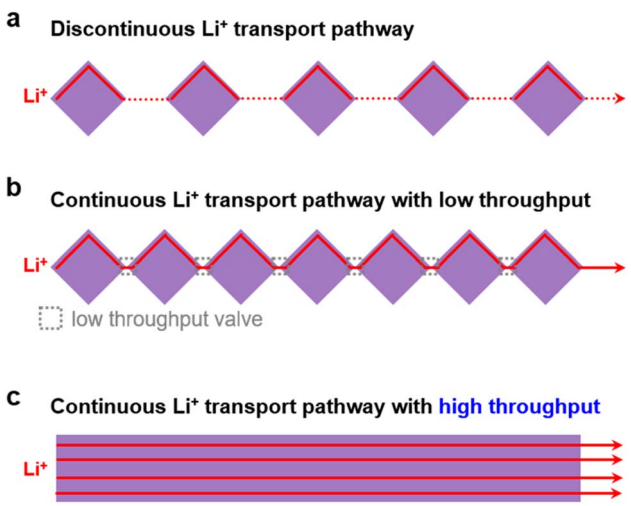

Fig. 1 The comparison of possible Li^+ transport pathways in various MOF-based CSEs. Schematic illustration of Li^+ transport pathways in CSEs with (a) randomly distributed MOF particles, (b) closely packed MOF particle-based chains reported recently, and (c) aligned MOF arrays proposed in this study. Compared with randomly distributed MOF particles, closely packed MOF chains offer a more continuous Li^+ transport pathway, but suffer from low throughput. Meanwhile, the proposed MOF arrays are free of crossing junctions with high throughput, thus enabling rapid Li^+ transport.

However, as shown in Fig. 1a, upon simply mixing MOF particles with SPEs, the MOF particles are isolated from each other which results in a discontinuous Li^+ transport pathway, leading to inhomogeneous ion transport with insufficient ionic conductivity.[29] Recently, to overcome the issues of randomly distributed MOF particles in CSEs, many research efforts have been devoted to reducing the distance between discrete MOF particles with the aim of building a continuous ion transport pathway between MOFs[30–34] (Fig. 1b). For instance, by growing a MOF (*i.e.*, Zr-BPDC-2SO_3H) on bacterial cellulose nanofibers, a continuous ion transport network was built with the aid of propylene carbonate solvent (17.63 wt%), which leads to a high ionic conductivity of 7.88×10^{-4} S cm^{-1} at 25 °C.[32] Later on, by *in situ* growth of densely packed MOFs (*i.e.*, ZIF-8) on polyacrylonitrile fibers and then encapsulating an ionic liquid (IL) in the MOF pores, our group developed a MOF/IL-based CSE with a high ionic conductivity of 2.57×10^{-4} S cm^{-1} and a high Li^+ transference number of 0.59.[34] However, despite the successful construction of continuous Li^+ transport networks with a significantly reduced distance, the point contact between different MOF particles would result in a low-throughput valve for Li^+ transport (Fig. 1b), leading to limited ionic conductivity improvement, unless an organic liquid is added (*e.g.*, solvent or IL). Therefore, it is of great importance to build continuous ion transport pathways with a high throughput and well-ordered structure to enable rapid Li^+ transport and a homogeneous Li^+ flux (Fig. 1c).

Herein, a vertically aligned MOF array was rationally designed and embedded into polymer electrolytes, with the aim of producing continuous Li^+ transport pathways with high throughput. As illustrated in Fig. 2, the ingenious structure of the MOF vertical array can regulate Li^+ transport along the shortest distance between the cathodes and anodes, promoting fast transport of Li^+. Furthermore, the abundant OMSs from the framework of the MOF array can capture the anions of lithium salts to offer a homogeneous Li^+ flux, which increases the Li^+ transference number and thereby suppresses the growth of Li dendrites. After permeating the MOF vertical array with PVDF electrolyte and PEO electrolyte on both sides, the resultant MOF array CSE with bilayer polymer electrolytes

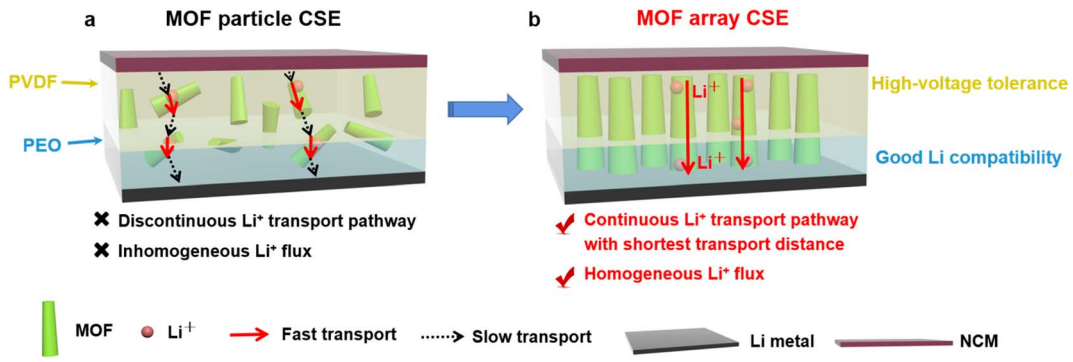

Fig. 2 Schematic illustrations of the Li^+ transport behaviors in (a) the MOF particle CSE and (b) MOF array CSE. The discrete MOF particles in the MOF particle CSE result in a discontinuous Li^+ transport pathway with an inhomogeneous Li^+ flux. Meanwhile, the MOF array CSE not only offers a continuous Li^+ transport pathway with the shortest transport distance between the cathode and anode, but also contributes to the homogeneous Li^+ flux.

demonstrates excellent interfacial compatibility towards both the high-voltage cathode and Li-metal anode. Consequently, markedly improved cycling performance with high CE was realized for a high-voltage Li||$LiNi_{1/3}Co_{1/3}Mn_{1/3}O_2$ (NCM) solid-state Li-metal battery at room temperature.

2. Experimental section

2.1. Synthesis of the MOF vertical array

2.6 g of 2-methylimidazole (mlm) and 1.17 g of $Co(NO_3)_2 \cdot 6H_2O$ were first dissolved separately in 80 mL of deionized water, respectively. After stirring vigorously for 5 min, the above two solutions were mixed quickly. Then, the separator with a ceramic coating layer (MA-EN-SE-0D) was fixed on the beaker wall and further immersed in the mixed solution for 5 h. After that, the separator with the MOF (*i.e.*, ZIF-67, $Co(mlm)_2$) array grown on the surface was taken out, washed with deionized water three times, and vacuum dried overnight. The mass loading of the grown MOF array was measured to be about 1.26 mg cm^{-2}, which was calculated by measuring the weight of the separator before and after growing the MOF array.

2.2. Fabrication of the MOF array CSE

0.1 g of PVDF and 0.1 g of lithium bis(trifluoromethanesulphonyl)imide (LiTFSI) were first mixed in 2.0 mL of *N*-methylpyrrolidone (NMP) solvent, and then stirred for 6 h at 50 °C to obtain a homogeneous solution (denoted as PVDF/LiTFSI). The above PVDF/LiTFSI solution was coated on a clean and smooth glass plate using a 400 μm doctor blade. The separator with the MOF array grown on top was then placed on the above PVDF/LiTFSI solution layer. A vacuum-assisted liquid filling method was employed to infiltrate the PVDF/LiTFSI into the MOF array, which was then vacuum dried at 80 °C for 24 h, and then the separator was peeled to afford the PVDF/MOF array. Thereafter, a mixed solution of PEO and LiTFSI (the molar ratio of [EO] : LiTFSI was 16 : 1) in acetonitrile with a concentration of 4.0 wt% PEO was coated on the surface of the PVDF/MOF array, and then subjected to vacuum drying at 80 °C for 24 h. The film was exfoliated from the glass substrate to yield a PVDF/MOF array/PEO CSE with bilayer polymer electrolytes on both sides (denoted as MOF array CSE). Finally, the film was cut into a circular disc with a diameter of 19 mm and stored in a glovebox prior to use.

2.3. Preparation of the NCM cathode

The NCM cathode was fabricated by mixing NCM powder with acetylene black and PVDF at a mass ratio of 80 : 12 : 8 using a Thinky mixer (AR-100). The slurry was then coated on a clean and smooth aluminum foil with a 100 μm doctor blade and dried under vacuum at 100 °C for 24 h. The electrode was cut into 12 mm discs and further dried under vacuum at 60 °C for 24 h, and then placed in a glovebox prior to use. The active mass loading of the NCM cathode was controlled at 2–3 mg cm^{-2}.

2.4. Electrochemical measurements

All the cells, including stainless-steel (SS)||SS, Li||Li, Li||SS, and Li||NCM, were assembled in an Ar-filled glovebox with a standard 2032-type coin cell configuration without any liquid electrolyte. Using a LAND CT2001A charge–discharge tester (Wuhan Jinnuo Electronic Co. Ltd), the charge–discharge tests of the Li||Li symmetrical and Li||NCM cells were carried out at different current densities. The Li||NCM cells were tested in the cut-off voltage range of 2.8–4.3 V. The ionic conductivity of the CSE was measured by AC impedance spectroscopy with the CSE being placed between two stainless-steel (SS) blocking electrodes. The electrochemical impedance spectra were measured at the temperature range from 303 to 343 K with an amplitude of 10 mV within the frequency range of 10^6 to 0.1 Hz. The ionic conductivity (σ) of the CSE was calculated using the following equation:

$$\sigma = \frac{R}{L \times S} \quad (1)$$

where R is the bulk resistance, L is the thickness of the CSE, and S is the area of the CSE.

The oxidation stability of the CSE was measured *via* linear sweep voltammetry (LSV) at a sweep rate of 1.0 mV s^{-1} from open circuit voltage (OCV) to 6.0 V using SS as the working electrode and lithium metal as both the reference and counter electrode. The Li^+ transference number (t_{Li^+}) was measured in a symmetric Li||Li cell according to the AC impedance and direct-current (DC) polarization (polarization voltage of 10 mV). The t_{Li^+} was calculated from the Bruce–Vincent–Evans equation:

$$t_{Li^+} = \frac{I_S \times (\Delta V - I_0 R_0)}{I_0 \times (\Delta V - I_S R_S)} \quad (2)$$

where I_0 and I_s are the initial current and the steady state current, R_0 and R_s are charge-transfer resistance before and after polarization for 7200 s, and ΔV is the applied polarization voltage (ΔV = 10 mV). The ionic conductivity, LSV, and Li^+ transference number measurements were performed using a VMP3 potentiostat (Bio-Logic).

2.5. COMSOL simulation

The distribution of Li^+, $TFSI^-$, and electric potential through the CSEs was investigated based on the finite element method (FEM)[35] using COMSOL Multiphysics. Two physical models of electrostatics and transport of diluted species based on the partial differential equations were coupled to conduct FEM simulation. The CSEs were built into a two-dimensional plane model, where the upper and lower surfaces were the contacted boundaries between the CSEs and Li metal electrodes. The migration of Li^+ and $TFSI^-$ was described by the Nernst–Planck equation. The diffusion coefficients of Li^+ and $TFSI^-$ in the MOF array CSE were 7.48 × 10^{-10} cm^2 S^{-1} and 6.12 × 10^{-10} cm^2 S^{-1}, respectively. For the MOF particle CSE, the diffusion coefficients of Li^+ and $TFSI^-$ were 2.81 × 10^{-10} cm^2 S^{-1} and 9.40 × 10^{-10} cm^2 S^{-1}, respectively. Current density was set as 0.2 mA cm^{-2} and a temperature of 303 K was applied.

3. Results and discussion

3.1. Rational design and fabrication of the MOF array CSE

Introducing crystalline MOFs as fillers into polymeric electrolytes has been regarded as a promising strategy to achieve high performance CSEs, in which the high specific surface areas of MOFs can facilitate contact with the polymer to reduce the interfacial resistance, the OMSs of MOFs can anchor anions of Li salts to promote rapid Li^+ transport and high Li^+ transference, and the periodically ordered channels of MOFs are favorable for generating a homogeneous Li^+ flux to induce homogeneous Li^+ plating/stripping. However, due to the discrete MOF particles in the polymeric matrix (Fig. 2a), Li^+ was primarily transported *via* MOF-to-polymer-to-MOF, which leads to high interfacial resistance and sluggish Li^+ transport.

As shown in Fig. 2b, aiming to build a continuous Li^+ transport pathway with the shortest transport distance between the cathode and anode, a MOF vertical array-based CSE was rationally designed that is free of crossing junctions with a low Li^+ migration barrier. The procedure to fabricate the MOF array CSE with bilayer polymer electrolytes is schematically shown in Fig. 3a. The separator with a ceramic coating layer serves as an excellent substrate for the growth of the MOF (*i.e.*, ZIF-67) vertical array. The top view scanning electron microscopy (SEM) image demonstrates that the MOF array with a typical vertically aligned morphology was uniformly grown on the separator (Fig. 3b), and the thickness of the MOF array was about 17 μm according to the cross-sectional SEM image (Fig. 3c), which is expected to offer continuous and rapid ion transport pathways. The X-ray diffraction (XRD) pattern of the MOF array/separator well matches with those of the pristine separator and pure MOF particle (*i.e.*, ZIF-67, Fig. S1†), which is also consistent with earlier work in the literature.[36,37] In addition, the corresponding elemental mapping images in Fig. S2 and S3† display a homogeneous elemental distribution of Co, C, and N. These results demonstrate the successful construction of the ZIF-67 vertical array on the separator substrate.

The MOF array/separator is then infiltrated with PVDF by doctor-blading PVDF/LiTFSI solution on a piece of glass plate and then placing the MOF/separator on the solution film with the MOF array side facing the solution. With the assistance of a vacuum, the voids within the MOF array were permeated through with PVDF/LiTFSI. To improve the interfacial compatibility of the CSE with the Li-metal anode, an additional PEO electrolyte layer was then cast on the PVDF/MOF array. The MOF array CSE with a hierarchical structure was finally obtained with a 15 μm thick PVDF layer and a 5.0 μm thick PEO layer permeating the MOF array (Fig. 3d), where the MOF array is expected to provide continuous and shortest Li^+ transport pathways, the high-voltage tolerance PVDF layer can be well compatible with the high-voltage cathode, and the PEO layer is expected to be well compatible with the Li-metal anode. For comparison, the CSE with randomly distributed MOF particles (denoted as MOF particle CSE) with similar bilayer polymer electrolytes was also prepared (Fig. S4†). The mass loading of the MOF in both the MOF array CSE and MOF particle CSE was

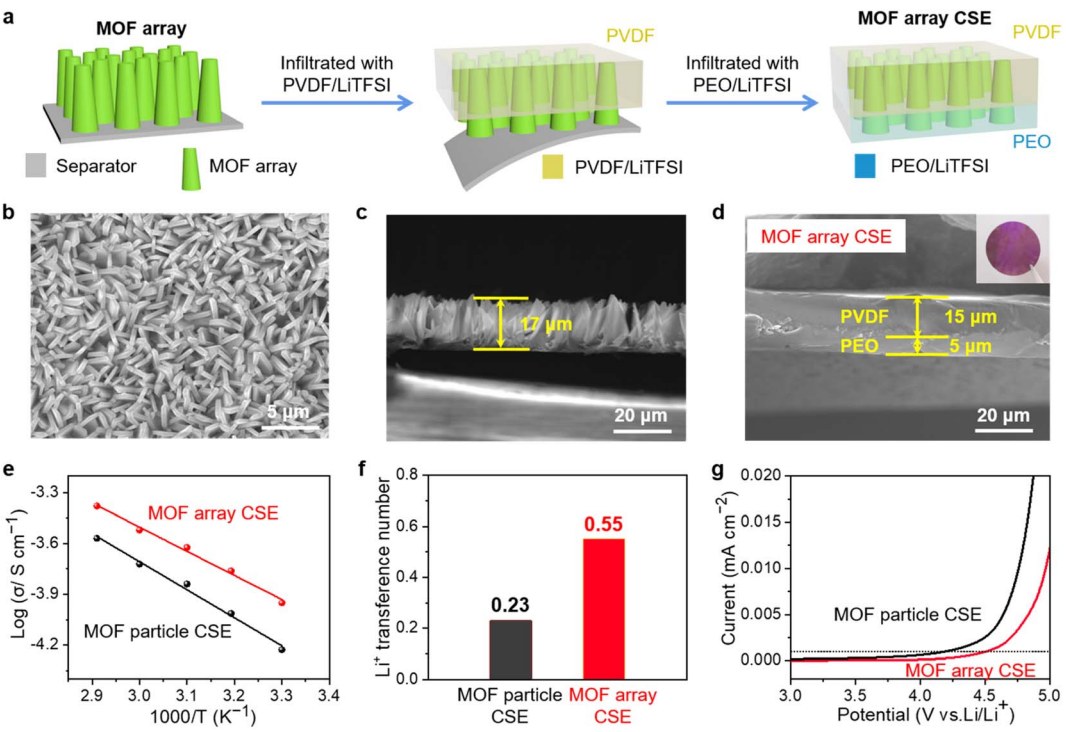

Fig. 3 Preparation and characterization of the CSEs. (a) Schematic procedure to fabricate the MOF array CSE. (b) Top view and (c) cross-sectional view SEM images of the MOF array grown on the separator. (d) Cross-sectional view of the MOF array CSE with bilayer polymer electrolytes. (e) Temperature-dependent ionic conductivities, (f) Li^+ transference numbers, and (g) oxidative stabilities of the MOF particle CSE and MOF array CSE.

controlled at ~1.25 mg cm^{-2}. From the SEM images in Fig. S5,† although there are some protrusions on the surface resulting from the vertical growth of the MOF array, the MOF array CSE was thoroughly infiltrated with PVDF/LiTFSI and PEO/LiTFSI. Furthermore, since a rigorous drying protocol was applied during the fabrication, we assume that neither the MOF array CSE nor MOF particle CSE contains any liquid, which was verified by the negligible weight loss before 225 °C during the thermogravimetric analysis (TGA) test (Fig. S6†).

3.2. Physicochemical properties of the MOF array CSE

The ionic conductivity is the primary parameter to evaluate the properties of CSEs for their practical application in solid-state Li-metal batteries, which was calculated from the AC impedance spectra. As shown in Fig. S7,† the ionic conductivity of the MOF array CSE without any liquid electrolyte was up to 1.12 × 10^{-4} S cm^{-1} at 30 °C, which is one order of magnitude higher than that of the MOF particle CSE (5.92 × 10^{-5} S cm^{-1}), indicating that the structure of the MOF vertical array with continuous and shortest ion transport pathways can evidently promote Li$^+$ transport. Furthermore, the activation energies (E_a) of the CSEs can be obtained from the Arrhenius equation. As shown in Fig. 3e, the E_a of the MOF array CSE was calculated to be 0.23 eV, which is lower than that of the MOF particle CSE (0.32 eV), indicating that a lower Li$^+$ migration energy barrier was realized in the MOF array CSE. The high ionic conductivity and low energy barrier for Li$^+$ migration in the MOF array CSE can be ascribed to the continuous ion transport pathways and shortest transport distance offered by the MOF array structure (Fig. 2b), favoring its application at room temperature. In contrast, the poor interfacial contact obtained through physically mixing MOF particles with the polymer electrolyte CSE results in a discontinuous ion transport pathway and hinders Li$^+$ migration, leading to low ionic conductivity and a high migration barrier (Fig. 2a).

According to the space-charge model demonstrated by Chazalviel,[38,39] lithium dendrites would grow when the Li$^+$ concentration on the surface of the electrode falls to zero at a high current density. The initial time of lithium dendrite growth is called Sand's time (τ), which empirically relies on the electron and Li$^+$ transference number (t_{Li}^+). A higher t_{Li}^+ would generate a higher limiting current that postpones the Sand's time, inhibiting the growth of lithium dendrites. Thus, as shown in Fig. 3f and S8,† the t_{Li}^+ was evaluated by the AC impedance and direct-current (DC) polarization. The t_{Li}^+ of the MOF array CSE was calculated to be 0.55, which is much higher than that of the MOF particle CSE (0.23). This was attributed to the continuous ion transport pathways with high throughput and the shortest transport distance possessed by the MOF array that promotes the rapid transport of Li$^+$, in addition to the

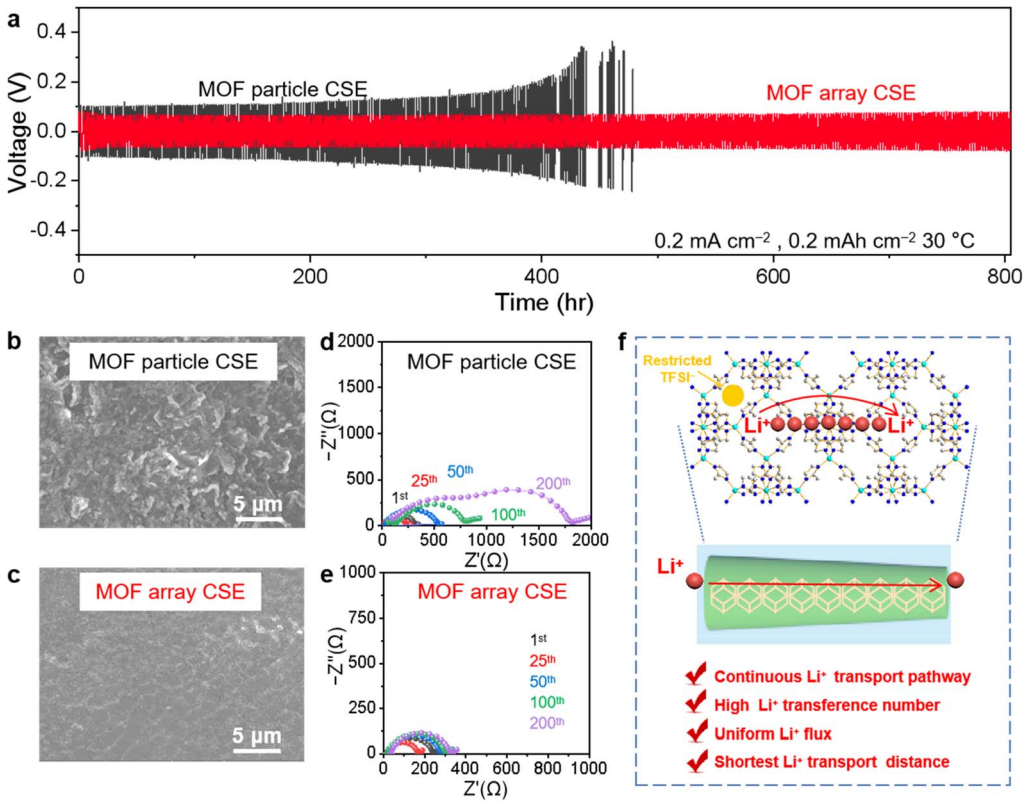

Fig. 4 Li plating/stripping stability. (a) Long-term cycling stability of symmetric Li||Li cells at a current density of 0.2 mA cm^{-2} for 0.2 mA h cm^{-2} at 30 °C. SEM images of Li-metal recovered from symmetric Li||Li cells using (b) the MOF particle CSE and (c) MOF array CSE after 200 cycles. Electrochemical impedance spectra of symmetric Li||Li cells using (d) the MOF particle CSE and (e) MOF array CSE after different number of cycles at 30 °C. (f) Schematic illustration of the ion transport behavior with a MOF array CSE, where the MOF array offers a continuous and rapid ion transport pathway with the shortest distance, leading to a homogeneous Li$^+$ flux and high Li$^+$ transference number.

abundant open metal sites and sieving effect offered by the MOF that can effectively restrict the $TFSI^-$ anion.

Furthermore, the electrochemical stability window of CSEs at room temperature was crucial for their application in high-voltage lithium batteries, which was measured by LSV. As shown in Fig. 3g, the MOF array CSE shows a high oxidation potential of 4.53 V, which is much higher than that of the MOF particle CSE (4.19 V) defined at 0.001 mA cm^{-2}. The superior oxidation stability of the MOF array CSE was attributed to the continuous ion transport pathway with high throughput and the shortest transport distance offered by the MOF array, enabling the majority of charges to travel along the continuous MOF pathways while minimizing the charge transport across the polymer matrixes.

3.3. Homogeneous Li deposition

The Li||Li symmetric cells using various CSEs were configured and tested to evaluate the long-term electrochemical stability and polarization during the Li plating/stripping process. As shown in Fig. 4a, after three activation cycles at the current density of 0.1 mA cm^{-2} with each plating/stripping procedure of 1 h, the Li||Li symmetric cell using the MOF particle CSE experiences an apparent short circuit after about 400 h at a current density of 0.2 mA cm^{-2} for 0.2 mA h cm^{-2} due to the overgrowth of lithium dendrites, while the cycle life was extended to over 800 h with a small and steady polarization voltage of 72 mV for that using the MOF array CSE. This result suggests that the MOF array CSE with continuous and high throughput Li^+ transport pathways could markedly regulate the homogeneous Li^+ deposition, which was confirmed by the flat and smooth surface of the lithium metal anode without obvious lithium dendrites after 100 h from the SEM image in Fig. 4c. In contrast, the lithium metal anode cycled using the MOF particle CSE displays a rough surface with bushy lithium dendrites, as shown in the SEM image in Fig. 4b. Moreover, compared with the significantly increased interfacial impedance in the symmetric Li||Li cell using the MOF particle CSE during cycling (Fig. 4d), the interfacial impedance of the cell coupled with the MOF array CSE exhibits a negligible increase during cycling (Fig. 4e), indicating its excellent interfacial stability. Furthermore, the Li||Li symmetric cells using the MOF array CSE can also support the stable cycling at high current densities (Fig. S9†), *i.e.*, more than 450 h at 0.3 mA cm^{-2} with a capacity of 0.3 mA h cm^{-2} and more than 300 h at 0.5 mA cm^{-2} with a capacity of 0.5 mA h cm^{-2}, respectively.

These results demonstrate that constructing continuous and high throughput Li^+ transport pathways based on the MOF array with a high aspect ratio is favorable for realizing dendrite-free Li plating/stripping, owing to the following reasons as schematically summarized in Fig. 4f: (1) due to the high aspect ratio of the MOF array, Li^+ could move rapidly along the long-range and periodically ordered channels; (2) the MOF array as the homogeneous filler possesses ion transport pathways with high throughput and the shortest distance giving rise to a homogeneous Li^+ flux, thereby regulating homogeneous Li^+ deposition; (3) the microporous structure and abundant OMSs within the MOF could restrict the $TFSI^-$ anion to increase Li^+ transference number, therefore suppressing the growth of lithium dendrites and resulting in a dendrite-free Li plating/stripping.

To further shed light on the ion transport trajectory in the MOF array CSE, the distributions of Li^+, $TFSI^-$, and electric field in the Li||Li symmetric cell were simulated by COMSOL Multiphysics. As shown in Fig. 5a and b, both Li^+ and $TFSI^-$ show small concentration gradients during the process of Li^+ plating in the MOF array CSE, indicating a homogeneous Li^+ flux, which was primarily ascribed to its high $t_{Li}{}^+$ as well as continuous and

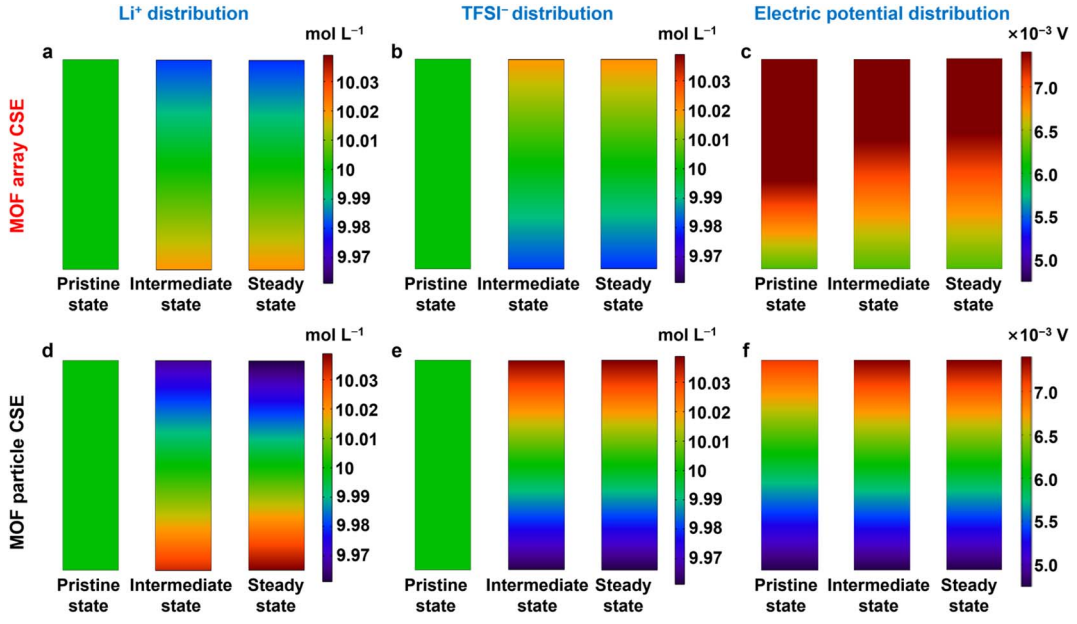

Fig. 5 COMSOL simulation results. The Li^+, $TFSI^-$, and electric potential distribution in (a–c) the MOF array CSE and (d–f) MOF particle CSE at pristine, intermediate, and steady states during Li^+ deposition at a current density of 0.2 mA cm^{-2}.

rapid Li^+ transport pathways. Because of the uniform distribution of Li^+ and $TFSI^-$, a small potential field is also observed for the MOF array CSE (Fig. 5c), enabling uniform and dendrite-free Li deposition. In contrast, the MOF particle CSE shows large concentration gradients for Li^+ and $TFSI^-$ as well as a large potential field (Fig. 5d–f), which results in uneven Li^+ deposition and rapid growth of lithium dendrites.

3.4. Stable operation of the high-voltage Li||NCM cell

The superiority of the MOF array CSE with continuous ion transport pathways and a hierarchical structure is eventually tested in high-voltage Li||NCM cells at 30 °C with a cutoff voltage of 2.8–4.3 V. As shown in Fig. 6a, the Li||NCM cell using the MOF array CSE delivers excellent rate capability, where the discharge capacities were 154, 146, 128, and 105 mA h g^{-1} at 0.1, 0.2, 0.5, and 1C, respectively (1C = 160 mA h g^{-1}). When the current density came back to 0.2C, the discharge capacity recovered to 148 mA h g^{-1}, indicating its excellent rate capability at room temperature, which could be attributed to its high ionic conductivity and high $t_{Li}{}^+$ as well as very thin nature of the CSE (~20 μm). In sharp contrast, the Li||NCM cell using the MOF particle CSE shows lower discharge capacities at various current densities. Furthermore, the Li||NCM cell using the MOF array CSE also shows lower over-potentials (*e.g.*, 416 mV at 1C) than that using the MOF particle CSE (560 mV at 1C) in charge–discharge curves (Fig. 6b and S10†).

The long-term cycling performance of the Li||NCM cells was also tested. As shown in Fig. 6c, the Li||NCM cell using the MOF array CSE displays a stable cycling performance with an initial discharge capacity of 137 mA h g^{-1} and a capacity retention of 75% after 300 cycles, outperforming most of the reported high-voltage cells (*i.e.*, >4.0 V) using MOFs/polymer based CSEs without any liquid (Table S1†). In contrast, the Li||NCM cell using the MOF particle CSE can only survive for 160 cycles, which may be ascribed to its poor oxidative stability. Furthermore, the surface morphology of the cycled lithium metal anode after 100 cycles was also investigated and is shown in Fig. 6c. The cycled lithium metal anode using the MOF array CSE exhibits a smooth and dendrite-free morphology, while that using the MOF particle CSE displays a massive porous and mossy-like morphology, indicating that the growth of the lithium dendrite has been effectively prevented by the deliberate construction of the MOF array with continuous and rapid

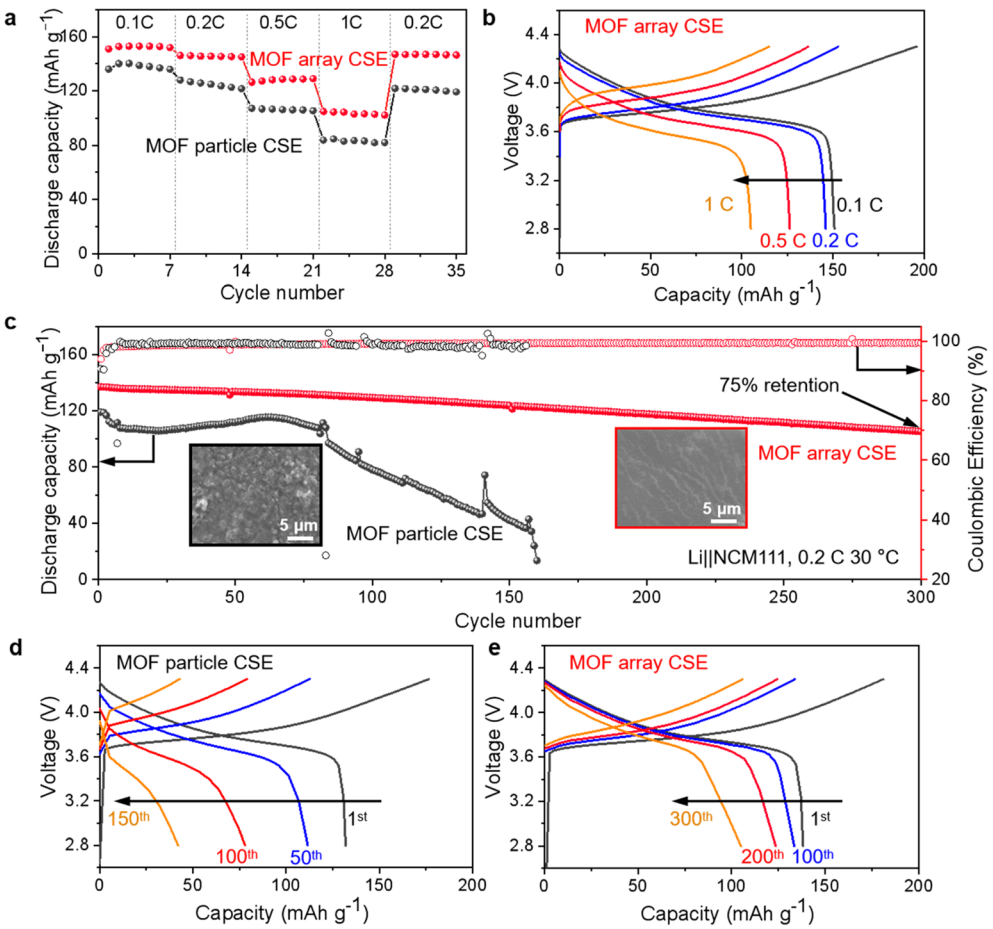

Fig. 6 Electrochemical performance of the Li||NCM cells at 30 °C. (a) Rate performance of Li||NCM cells using the MOF particle and MOF array CSEs. (b) Selected charge–discharge curves of the Li||NCM cell using the MOF array CSE at different current densities. (c) Cycling performance and (d and e) selected charge–discharge curves of Li||NCM cells using the MOF particle and MOF array CSEs with a cut-off voltage of 2.8–4.3 V at 0.2C.

Li^+ transport pathways, a high Li^+ transference number, and homogeneous Li^+ flux.

Moreover, compared with that using the MOF particle CSE in Fig. 6d, the Li‖NCM cell using the MOF array CSE exhibits no obvious change in the voltage polarization during cycling (Fig. 6e), suggesting its excellent interfacial compatibility towards both the cathode and anode, which was further evidenced by the electrochemical impedance measurement (Fig. S11†). In contrast to the cell using the MOF particle CSE, whose interfacial resistance drastically increased after 10 cycles, the cell using the MOF array CSE displays impressively steady interfacial resistance even after 300 cycles. Additionally, the Li‖NCM cell using the MOF array CSE also demonstrates stable cycling at a high current density of 0.5C at 60 °C, while the cell using the MOF particle CSE exhibits rapid capacity decay (Fig. S12†).

4. Conclusions

In summary, a MOF array CSE was delicately designed by embedding a vertical MOF array with bilayer polymer electrolytes to overcome the longstanding challenges of large Li^+ migration barrier, inhomogeneous Li deposition, and high-voltage incompatibility. The MOF vertical array not only offers continuous ion transport pathways with high throughput, but also minimizes the Li^+ transport distance between the cathode and anode. Furthermore, the utilization of the MOF array with open metal sites and periodically ordered channels can restrict anion transport to achieve a homogeneous Li^+ flux with a high Li^+ transference number (0.55). Moreover, the unique bilayer structure is demonstrated to stabilize both the Li-metal anode and high-voltage cathode. Benefiting from the above merits, the resulting MOF array CSE allows the stable cycling of a Li‖Li symmetric cell for over 800 h and high-voltage Li‖NCM cell at room temperature. This work highlights the great prospect for constructing a MOF array with continuous ion transport pathways and the shortest transport distance in CSEs, which opens up a new avenue for the development of high-performance solid-state batteries.

Conflicts of interest

There are no conflicts to declare.

Acknowledgements

This work was supported by the National Natural Science Foundation of China (No. 22005108, 22208118), Natural Science Foundation of Guangdong Province (No. 2021A1515110655, 2022B1515020005), and Department of Science and Technology of Guangdong Province (No. 2021A0505030063, 2020B0101030005).

References

1 D. T. Boyle, X. Kong, A. Pei, P. E. Rudnicki and Y. Cui, *ACS Energy Lett.*, 2020, **5**, 701–709.
2 X. B. Cheng, R. Zhang, C. Z. Zhao and Q. Zhang, *Chem. Rev.*, 2017, **117**, 10403–10473.
3 S. Jin, Y. Ye, Y. Niu, Y. Xu, H. Jin, J. Wang, Z. Sun, A. Cao, X. Wu and Y. Luo, *J. Am. Chem. Soc.*, 2020, **142**, 8818–8826.
4 X. R. Chen, B. C. Zhao, C. Yan and Q. Zhang, *Adv. Mater.*, 2021, **33**, 2004128.
5 J. F. Ding, R. Xu, X. X. Ma, Y. Xiao, Y. X. Yao, C. Yan and J. Q. Huang, *Angew. Chem., Int. Ed.*, 2022, **61**, e202115602.
6 B. Liu, J. G. Zhang and W. Xu, *Joule*, 2018, **2**, 833–845.
7 K. Amine, R. Kanno and Y. Tzeng, *MRS Bull.*, 2014, **39**, 395–401.
8 X. Wu, J. L. Wang, D. Fei, X. L. Chen, E. Nasybulin, Y. H. Zhang and J. G. Zhang, *Energy Environ. Sci.*, 2014, **7**, 513–537.
9 R. Chen, Q. Li, X. Yu, L. Chen and H. Li, *Chem. Rev.*, 2020, **120**, 6820–6877.
10 J. C. Bachman, S. Muy, A. Grimaud, H. H. Chang and Y. Shao-Horn, *Chem. Rev.*, 2015, **116**, 140–162.
11 J. Wan, J. Xie, D. G. Mackanic, W. Burke and Y. Cui, *Mater. Today Nano*, 2018, **4**, 1–16.
12 S. X. Xia, X. S. Wu, Z. C. Zhang, Y. Cui and W. Liu, *Chem*, 2019, **5**, 753–785.
13 Y. Zheng, Y. Z. Yao, J. H. Ou, M. Li and Z. W. Chen, *Chem. Soc. Rev.*, 2020, **49**, 8790–8839.
14 D. Zhou, D. Shanmukaraj, A. Tkacheva, M. Armand and G. Wang, *Chem*, 2019, **5**, 2326–2352.
15 X. Zhan, S. Lai, M. P. Gobet, S. G. Greenbaum and M. Shirpour, *Phys. Chem. Chem. Phys.*, 2018, **20**, 1447–1459.
16 Y. Sun, K. Suzuki, K. Hara, S. Hori, T. A. Yano, M. Hara, M. Hirayama and R. Kanno, *J. Power Sources*, 2016, **324**, 798–803.
17 J. R. Xu, L. L. Liu, N. Yao, F. Wu and L. Q. Chen, *Mater. Today Nano*, 2019, **8**, 100048.
18 D. Zhou, M. Y. Zhang, F. Sun, T. Arlt and M. Winter, *Nano Energy*, 2020, **77**, 105196.
19 S. S. Chi, Y. Liu, N. Zhao, X. Guo, C. W. Nan and L. Z. Fan, *Energy Storage Mater.*, 2019, **17**, 309–316.
20 O. Borodin and G. D. Smith, *Macromolecules*, 2006, **39**, 1620–1629.
21 S. H. Cheng, K. He, Y. Liu, J. W. Zha, M. Kamruzzaman, L. W. Ma, Z. Dang and C. Y. Chung, *Electrochim. Acta*, 2017, **253**, 430–438.
22 M. Nishiura, M. Kono, N. Namegaya and Y. Matsuda, *Electrochem. Solid-State Lett.*, 1998, **1**, 246–248.
23 X. Han, Y. Gong, K. K. Fu, X. He, G. T. Hitz, J. Dai, A. Pearse, B. Liu, H. Wang, G. Rubloff, Y. Mo, V. Thangadurai, E. D. Wachsman and L. Hu, *Nat. Mater.*, 2017, **16**, 572–579.
24 J. Liang, J. Luo, Q. Sun, X. Yang and X. Sun, *Energy Storage Mater.*, 2019, **21**, 308–334.
25 Q. Zhou, J. Ma, S. Dong, X. Li and G. Cui, *Adv. Mater.*, 2019, **31**, 1902029.
26 S. Bai, Y. Sun, J. Yi, Y. He, Y. Qiao and H. Zhou, *Joule*, 2018, **2**, 2117–2132.
27 W. Xu, X. Pei, C. S. Diercks, H. Lyu and O. M. Yaghi, *J. Am. Chem. Soc.*, 2019, **141**, 17522–17526.
28 R. Zhao, Y. Wu, Z. Liang, L. Gao, W. Xia, Y. Zhao and R. Zou, *Energy Environ. Sci.*, 2020, **13**, 2386–2403.

29 L. Chen, K. Ding, K. Li, Z. Li, X. Zhang, Q. Zheng, Y.-P. Cai and Y.-Q. Lan, *EnergyChem*, 2022, **4**, 100073.
30 L. Du, B. Zhang, W. Deng, Y. Cheng, L. Xu and L. Mai, *Adv. Energy Mater.*, 2022, **12**, 2200501.
31 Z. Li, S. Wang, J. Shi, Y. Liu, S. Zheng, H. Zou, Y. Chen, W. Kuang, K. Ding, L. Chen, Y.-q. Lan, Y.-p. Cai and Q. Zheng, *Energy Storage Mater.*, 2022, **47**, 262–270.
32 Q. Zeng, J. Wang, X. Li, Y. Ouyang, W. He, D. Li, S. Guo, Y. Xiao, H. Deng, W. Gong, Q. Zhang and S. Huang, *ACS Energy Lett.*, 2021, **6**, 2434–2441.
33 Q. Zhang, B. Liu, J. Wang, Q. Li, D. Li, S. Guo, Y. Xiao, Q. Zeng, W. He, M. Zheng, Y. Ma and S. Huang, *ACS Energy Lett.*, 2020, **5**, 2919–2926.
34 X.-L. Zhang, F.-Y. Shen, X. Long, S. Zheng, Z. Ruan, Y.-P. Cai, X.-J. Hong and Q. Zheng, *Energy Storage Mater.*, 2022, **52**, 201–209.
35 J. Newman, K. E. Thomas, H. Hafezi and D. R. Wheeler, *J. Power Sources*, 2003, **119**, 838–843.
36 G. Fang, J. Zhou, C. Liang, A. Pan, C. Zhang, Y. Tang, X. Tan, J. Liu and S. Liang, *Nano Energy*, 2016, **26**, 57–65.
37 C. Guan, W. Zhao, Y. Hu, Z. Lai, X. Li, S. Sun, H. Zhang, A. K. Cheetham and J. Wang, *Nanoscale Horiz.*, 2017, **2**, 99–105.
38 J. N. Chazalviel, *Phys. Rev. A*, 1991, **42**, 7355–7367.
39 X. Zhang, A. Wang, X. Liu and J. Luo, *Acc. Chem. Res.*, 2019, **52**, 3223–3232.